Chinese Physics Letters

LETTER

State-Resolved Ar II Population Distributions under Femtosecond Strong-Field Excitation

Cite as: Di Wang *et al*. 2026 *Chin. Phys. Lett.* **43** 060301

DOI CSTR

Recommended Articles

Angular-Momentum-Resolved Rydberg State Population of Argon Ions in Strong Laser Fields
Zhigang Zheng, Di Wang, Mingyue Wang, Li Wang, Xu Sun, Jing Zhao, Zhihui Lv, Xiaowei Wang, and Zengxiu Zhao
Chin. Phys. Lett. **42**, 053702 (2025)

Rydberg-State Excitation and Ionization of Argon Atoms Subject to Strong Circularly Polarized Two-Color Few-Cycle Laser Fields
Zhiqiang Wang, Wei Quan, Yanlan Wang, Xiaolei Hao, Jing Chen, and Xiaojun Liu
Chin. Phys. Lett. **42**, 053701 (2025)

Quantum State-Resolved Nonadiabatic Dynamics of the H+NaF → Na+HF Reaction
Ye Mao, Hanghang Chen, Zijiang Yang, Bayaer Buren, and Maodu Chen
Chin. Phys. Lett. **41**, (2024)

***In situ* Measurement of Intense Optical Fields via Strong Field Ionization**
Fan Xiao, Li Wang, Guangru Bai, Zhigang Zheng, Xu Sun, Tiefeng Ji, Yuchen Sun, Jiacan Wang, Xiaowei Wang, and Zengxiu Zhao
Chin. Phys. Lett. **42**, 043701 (2025)

Generation of Circularly Polarized Strong-Field Terahertz Waves
Jiang-Hao Li, Hong-Ting Xiong, De-Yin Kong, Wei-Peng Zhao, Shao-Jie Liu, Bao-Gang Quan, and Xiao-Jun Wu
Chin. Phys. Lett. **41**, 124201 (2024)

iopscience.iop.org/cpl | cpl.iphy.ac.cn

A series journal of Chinese Physical Society distributed by IOP Publishing

Chinese Physics Letters

Chin. Phys. Lett. **43** 060301 (2026)

LETTER

DOI: 10.1088/0256-307X/43/6/060301
CSTR: 32039.14.0256-307X.43.6.060301

State-Resolved Ar II Population Distributions under Femtosecond Strong-Field Excitation

Di Wang(王迪)[1], Yuxuan Zhang(张宇璇)[1], Zhigang Zheng(郑志刚)[1], Mingyue Wang(王铭悦)[1], Zhihui Lv(吕治辉)[1,2], Li Wang(王力)[1,2], Xiaowei Wang(王小伟)[1,2], Dongwen Zhang(张栋文)[1,2], Jing Zhao(赵晶)[1,2,*], and Zengxiu Zhao(赵增秀)[1,2,*]

[1]College of Science, National University of Defense Technology, Changsha 410073, China
[2]Hunan Key Laboratory of Extreme Matter and Applications, National University of Defense Technology, Changsha 410073, China

[*]Corresponding authors. Email: jzhao@nudt.edu.cn; zhaozengxiu@nudt.edu.cn

We measure spontaneous emission from Ar II ions produced by femtosecond strong-field excitation of argon and reconstruct state-resolved excited-state populations from selected emission lines spanning upper-level energies of ~19–23 eV above the Ar II ground state. The ionic-line intensities follow a power-law dependence on pulse energy and a non-monotonic dependence on gas pressure, and the extracted populations deviate significantly from a Boltzmann distribution. The deviation grows with increasing pulse energy, reflecting a stronger nonequilibrium character of the initial population prepared by the strong field, and weakens with increasing gas pressure, consistent with collisional redistribution driving the system toward thermal equilibrium. These results establish ionic fluorescence as a practical state-resolved probe of nonequilibrium population distributions in strong-field-ionized argon.

Recent strong-field studies have shown that ionization by femtosecond laser pulses prepares ions in multiple electronic channels with pronounced nonequilibrium populations and coherences [1–6]. These ions are produced and evolve through ionization, excitation, recollision-driven coupling, and subsequent collisions [7–10]. The resulting population distribution therefore retains information on both the strong-field preparation and the subsequent evolution of the ionic system. As attention has gradually shifted from the released electron to the residual ion [11–13], determining ionic excited-state distributions has become essential for testing strong-field dynamics and interpreting ultrafast spectroscopic observables.

Ionic dynamics have been investigated by a variety of ultrafast techniques, from momentum-resolved electron and ion measurements [14–19] and coherence-driven optical probes [11,20,21] to attosecond transient absorption and high-harmonic spectroscopy [12,13,22–26]. These methods predominantly access continuum observables or a limited number of bound-state pathways, making it challenging to extract population distributions over multiple ionic excited states. In contrast, spontaneous-emission spectroscopy, which has been widely applied in laser-driven gas diagnostics [27–29], offers complementary access to numerous excited levels in a single measurement, yet its potential for resolving state-specific ionic populations under strong-field excitation has not been fully exploited.

Fluorescence and emission spectroscopy have already been applied to characterize excited-state populations produced by intense femtosecond laser fields. For molecular ions, emission from species such as N_2^+ and CO^+ has been extensively analyzed to determine electronic and vibrational population distributions [30–34]. A similar approach applied to CO_2^+ has enabled orbital-resolved ionization studies via its characteristic fluorescence wavelengths [35,36]. Fluorescence from neutral atoms and molecules in femtosecond laser filaments has also been utilized for species-specific diagnostics [37,38]. Although excited-ion production and coherence-driven emission in intense femtosecond fields have been reported [9,39–41], systematic state-resolved population analysis across multiple ionic emission lines remains largely unexplored.

In this work, we measure Ar II fluorescence produced by femtosecond strong-field excitation of argon and reconstruct state-resolved excited-state populations of Ar II from selected emission lines spanning upper-level energies of ~19–23 eV above the Ar II ground state. The fluorescence intensity is found to follow a power-law dependence on pulse energy and a non-monotonic dependence on gas pressure. The extracted population distributions deviate significantly from a Boltzmann distribution, and their systematic evolution with pulse energy and gas pressure reveals the respective roles of strong-field preparation, collisional redistribution, and electron-ion recombination in shaping the nonequilibrium ionic population.

In the experiment, the laser system (Lancer-K13-2Reg) delivers 30-fs pulses centered at 800 nm at a repetition rate of 1 kHz, with pulse energies up to 2.2 mJ available at the interaction region. The estimated vacuum peak intensity is 6×10^{15} W/cm^2, reduced in practice by filament-induced focal shift and intensity clamping. The pulses are focused by a spherical lens ($f = 300$ mm) into a vacuum chamber filled with argon. Fluorescence from the interaction region is collected perpendicular to the laser propagation axis by two spherical lenses ($f = 100$ mm). The raw spectra are recorded by a spectrometer (Andor SR500i) at a spectral resolution of 0.03 nm and subjected to intensity calibration using a deuterium-halogen lamp. The pulse energy is varied by a half-wave plate and a wire-grid polarizer placed before the focusing lens, while the gas pressure is controlled independently by the chamber valve.

Using this setup, we record the background-subtracted and intensity-calibrated fluorescence spectrum in the wavelength range 360–520 nm, as shown in Fig. 1. Comparison with the NIST Atomic Spectra Database [44] identifies the observed features as predominantly Ar II spontaneous-emission lines. For isolated lines, the integrated intensity is obtained from $I_i = \int S(\varepsilon)\mathrm{d}\varepsilon$, where $S(\varepsilon)$ is the measured spectral signal at photon energy ε. For unresolved overlapping lines, the spectral profile is fitted with a pseudo-Voigt function [45,46],

$$S_{\mathrm{fit}}(\varepsilon) = \sum_i A_i \left[\mu_i \frac{\gamma_i^2}{(\varepsilon-\varepsilon_i)^2+\gamma_i^2} + (1-\mu_i)\exp\left(-\frac{(\varepsilon-\varepsilon_i)^2}{2\sigma_i^2}\right)\right], \quad (1)$$

where A_i is the amplitude, ε_i is the peak photon energy, γ_i is the Lorentzian half-width, σ_i is the Gaussian standard deviation, and μ_i is the mixing coefficient of the ith line. The line intensity is then

Received 23 March 2026; accepted 14 May 2026; published 17 June 2026

© 2026 Chinese Physical Society and IOP Publishing Ltd. All rights, including for text and data mining, AI training, and similar technologies, are reserved.

Check for updates

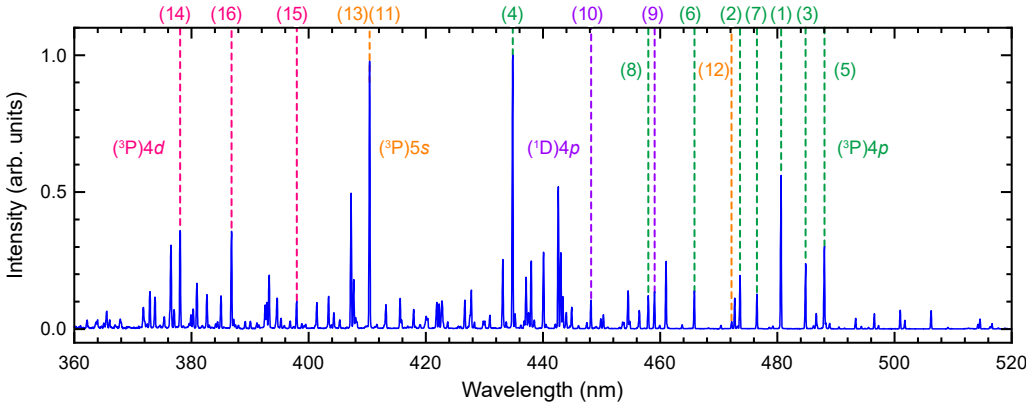

Fig. 1. Background-subtracted fluorescence spectrum of Ar II collected perpendicular to the laser propagation direction. The labeled lines are classified and numbered in ascending order of upper-level energy, as listed in Table 1. Lines (1)–(8) (green), (9)–(10) (purple), (11)–(13) (orange), and (14)–(16) (pink) correspond to the upper configurations $(^3P)4p$, $(^1D)4p$, $(^3P)5s$, and $(^3P)4d$, respectively. The common core configuration $3s^23p^4$ is omitted.

Table 1. Detailed information for the 16 selected Ar II fluorescence lines in the measured spectral range 360–520 nm [42–44]. The line numbers are arranged in ascending order of upper-level energy.

No.	Wavelength (nm)	Lower level $3s^23p^4$	Upper level $3s^23p^4$	RI	A_{ki} (10^7 s^{-1})	Upper-level energy (eV)
14	378.08	$(^3P)4p\ ^4D_{7/2}$	$(^3P)4d\ ^4D_{7/2}$	81	7.7	22.7729
16	386.85	$(^3P)4p\ ^4S_{3/2}$	$(^3P)4d\ ^4P_{5/2}$	166	14	23.1715
15	397.94	$(^3P)4p\ ^4S_{3/2}$	$(^3P)4d\ ^4P_{1/2}$	87	9.8	23.0823
13	410.38	$(^3P)4p\ ^2D_{5/2}$	$(^3P)5s\ ^2P_{3/2}$	158	13	22.7004
11	410.39	$(^3P)4p\ ^4D_{7/2}$	$(^3P)5s\ ^4P_{5/2}$	447	12	22.5148
4	434.81	$(^3P)4s\ ^4P_{5/2}$	$(^3P)4p\ ^4D_{7/2}$	1995	11.7	19.4945
10	448.18	$(^3P)3d\ ^2D_{5/2}$	$(^1D)4p\ ^2D_{5/2}$	646	4.55	21.4980
8	457.93	$(^3P)4s\ ^2P_{1/2}$	$(^3P)4p\ ^2S_{1/2}$	871	8.0	19.9725
9	458.99	$(^1D)4s\ ^2D_{3/2}$	$(^1D)4p\ ^2F_{5/2}$	25704	6.64	21.1270
6	465.79	$(^3P)4s\ ^2P_{3/2}$	$(^3P)4p\ ^2P_{1/2}$	1445	8.92	19.8011
12	472.16	$(^3P)4p\ ^4S_{3/2}$	$(^3P)5s\ ^4P_{3/2}$	32	1.5	22.5927
2	473.59	$(^3P)4s\ ^4P_{5/2}$	$(^3P)4p\ ^4P_{3/2}$	1000	5.80	19.2611
7	476.49	$(^3P)4s\ ^2P_{1/2}$	$(^3P)4p\ ^2P_{3/2}$	2344	6.4	19.8672
1	480.60	$(^3P)4s\ ^4P_{5/2}$	$(^3P)4p\ ^4P_{5/2}$	1820	7.80	19.2229
3	484.78	$(^3P)4s\ ^4P_{3/2}$	$(^3P)4p\ ^4P_{1/2}$	832	8.49	19.3053
5	487.99	$(^3P)4s\ ^2P_{3/2}$	$(^3P)4p\ ^2D_{5/2}$	2239	8.23	19.6800

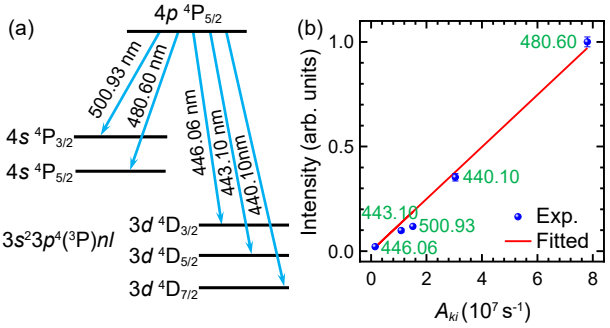

Fig. 2. (a) Transition diagram associated with the upper level $3s^23p^4(^3P)4p\ ^4P_{5/2}$ in the measured range 360–520 nm. (b) Dependence of the intensities of the five lines in (a) on their Einstein coefficients A_{ki}.

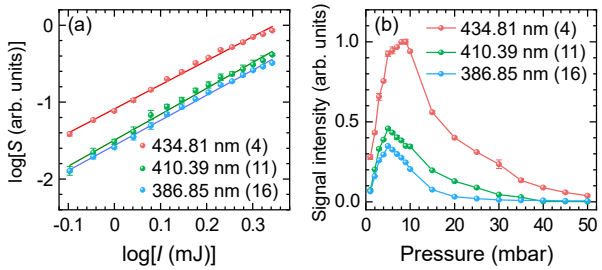

Fig. 3. (a) Pulse-energy dependence of the intensities of the 434.81,410.39, and 386.85 nm lines at 5 mbar, with fitted exponents of 3.13, 3.37, and 3.27, respectively. Symbols with error bars are experimental data, and the curves are power-law fits. (b) Gas-pressure dependence of the same three lines at 2.2 mJ.

obtained by integrating the fitted profile.

As a consistency check on the population extraction procedure, we consider five lines sharing the same upper level $3s^23p^4(^3P)4p\ ^4P_{5/2}$, as shown in Fig. 2(a). Their intensities scale linearly with the Einstein coefficient A_{ki}, consistent with the relation $I \propto A_{ki}N_k$ for a common upper-level population N_k, as shown in Fig. 2(b). This confirms that a consistent value of N_k is obtained from different decay channels and supports the identification of the detected fluorescence as spontaneous emission.

To investigate how experimental parameters affect the selective excitation of argon ions, we measure the dependence of the Ar II fluorescence signal on laser pulse energy and gas pressure. As shown in Fig. 3(a), the intensities of the representative lines increase monotonically with pulse energy and follow a power-law dependence with an exponent close to 3. An exponent of this magnitude would correspond to the number of photons absorbed only in the perturbative regime [38,47,48]. In the present strong-field regime, the observed exponent instead reflects the combined intensity dependence of tunneling ionization, recollision-induced excitation, and post-pulse relaxation

Table 2. Wavelengths and upper-level configurations of the 16 selected lines. Detailed spectroscopic information is given in Table 1.

No.	(1)	(2)	(3)	(4)	(5)	(6)	(7)	(8)	(9)	(10)	(11)	(12)	(13)	(14)	(15)	(16)
λ (nm)	480.60	473.59	484.78	434.81	487.99	465.79	476.49	457.93	458.99	448.18	410.39	472.16	410.38	378.08	397.94	386.85
Upper	(^{3}P)4p								(^{1}D)4p		(^{3}P)5s			(^{3}P)4d		
Level	$^4P_{5/2}$	$^4P_{3/2}$	$^4P_{1/2}$	$^4D_{7/2}$	$^2D_{5/2}$	$^2P_{1/2}$	$^2P_{3/2}$	$^2S_{1/2}$	$^2F_{5/2}$	$^2D_{5/2}$	$^4P_{5/2}$	$^4P_{3/2}$	$^2P_{3/2}$	$^4D_{7/2}$	$^4P_{1/2}$	$^4P_{5/2}$

rather than a specific photon order. Figure 3(b) shows that the representative line intensities also exhibit a non-monotonic dependence on gas pressure. At lower pressure, increasing the gas density raises both the ion yield produced during the laser interaction and the probability of post-pulse collisional excitation, resulting in stronger fluorescence. At higher pressure, collisional recombination of Ar II to neutral Ar and collisional quenching become increasingly important, and the ionic fluorescence correspondingly diminishes. This interpretation is qualitatively consistent with the enhancement of neutral-atom emission and suppression of ionic lines at higher pressure observed in our experiment. These intensity trends provide the experimental background for the population-distribution analysis below.

We then derive the populations of excited states from 16 lines originating from distinct upper levels (Table 2). For relative comparisons, the upper-level population is defined as $N_k = I/(g_k A_{ki})$, where I is the integrated line intensity, g_k is the degeneracy of the upper level, and A_{ki} is the Einstein coefficient. The A_{ki} values are all taken from the NIST Atomic Spectra Database and relevant literature [42–44], as detailed in Table 1. Figures 4(a)–4(c) show the relative populations as a function of upper-level energy E_k for three pulse energies at 5 mbar. For each pulse energy, the populations are normalized to the 480.60 nm line, which has the lowest upper-level energy, and compared with a Boltzmann distribution,

$$N_k \propto \exp\left(-\frac{E_k - E_1}{k_B T}\right), \tag{2}$$

where E_1 is the upper-level energy of the 480.60 nm line, k_B is the Boltzmann constant, and T is the equilibrium temperature corresponding to the reference Boltzmann distribution. Because the ions prepared by femtosecond strong-field excitation are in a nonequilibrium state, the fitted Boltzmann distribution is used here only as a reference for quantifying the degree of deviation under different conditions. We therefore focus on the fitting quality, characterized by the goodness of fit (R^2) and root-mean-square error (RMSE), rather than on the numerical value of T. Figure 4(d) shows that the relative populations increase systematically with pulse energy. Since the measurements in Fig. 4 are performed at 5 mbar, where collisional modification is comparatively weak, the extracted distributions are expected to more closely reflect the laser-prepared ionic population, while still containing a residual post-pulse contribution.

The measured populations deviate from a Boltzmann distribution at all pulse energies. Several high-lying levels ($E_k > 22$ eV) lie above the fitted curves, while some low-lying levels fall below, indicating that the excited-state populations cannot be described by a single Boltzmann distribution. The population excess is attributed in part to electron–Ar III recombination, which preferentially populates high-lying Ar II Rydberg states that then cascade into the observed levels, selectively enhancing their populations relative to the lower-energy states. This behavior is consistent with the ultrashort pulse duration, since the 30-fs interaction time is far shorter than typical collisional relaxation times, and consequently the initial population is established by the strong-field process before collisions can redistribute it toward equilibrium. More fundamentally, in the strong-field regime the production of each ionic excited state is governed by channel-specific ionization dynamics rather than by thermal equilibrium. The highly nonlinear dependence of the tunneling rate on the ionization threshold differs qualitatively from the Boltzmann factor, so that the initial population distribution is intrinsically nonthermal. In addition, high-lying levels lie closer to the ionization continuum, making them particularly susceptible to population enhancement via the recombination and cascade pathways discussed above. At 5 mbar the argon number density is of order 10^{17} cm^{-3}, giving a mean Ar II–Ar collision interval of ~30 ns, comparable to or longer than the spontaneous-emission lifetime of the observed Ar II transitions (~10–70 ns, $A_{ki} \sim 10^7$–10^8 s^{-1}). Most excited ions therefore decay radiatively before significant collisional redistribution occurs, and lifetime-dependent collisional quenching does not significantly bias the extracted population distribution under the present conditions. As shown in Figs. 4(e) and 4(f), the R^2 gradually decreases and the RMSE increases with rising pulse energy. This indicates increasingly pronounced deviations from a Boltzmann-like distribution at higher pulse energies, consistent with enhanced strong-field preparation and the stronger nonequilibrium character of the initial population.

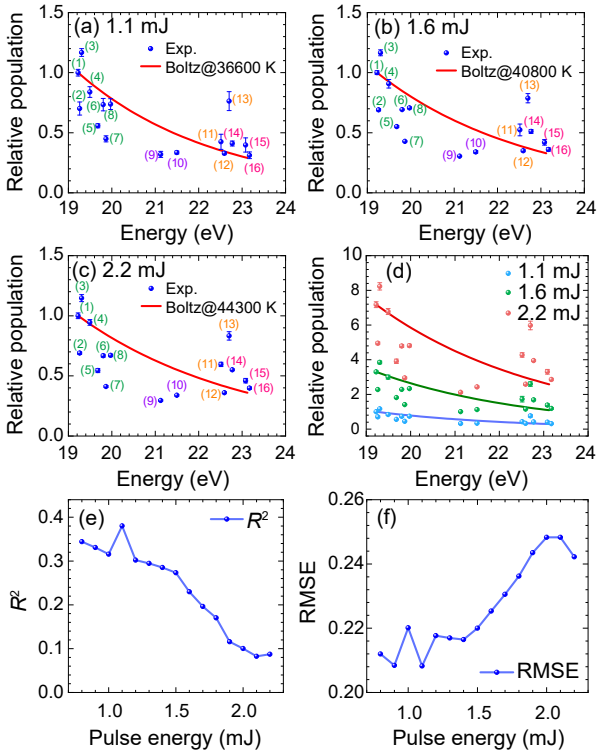

Fig. 4. Relative population distribution of 16 Ar II excited states at 5 mbar and pulse energies of (a) 1.1 mJ, (b) 1.6 mJ, and (c) 2.2 mJ. For each pulse energy, the populations are normalized to that of the 480.60 nm line. Blue symbols with error bars are experimental data, and red curves are Boltzmann fits. (d) Relative populations at different pulse energies, normalized to the population of the 480.60 nm line at 1.1 mJ. (e) Goodness of fit (R^2) at different pulse energies. (f) Root-mean-square error (RMSE) between fitted and experimental values at different pulse energies.

The pressure dependence of the population distribution is shown in Fig. 5. As the gas pressure increases, the deviation of the high-lying populations from the Boltzmann fits becomes weaker, indicating a gradual approach to a Boltzmann-like distribution. This trend suggests that increasing collision frequency promotes inter-level population redistribution after the pulse. At the same time, the pressure dependence in Fig. 3(b) and the population trend in Fig. 5(d) show that gas pressure also changes the total ionic yield contributing to the fluorescence signal. As shown in Figs. 5(e) and 5(f), the R^2 gradually increases with rising gas pressure, while the RMSE exhibits the opposite

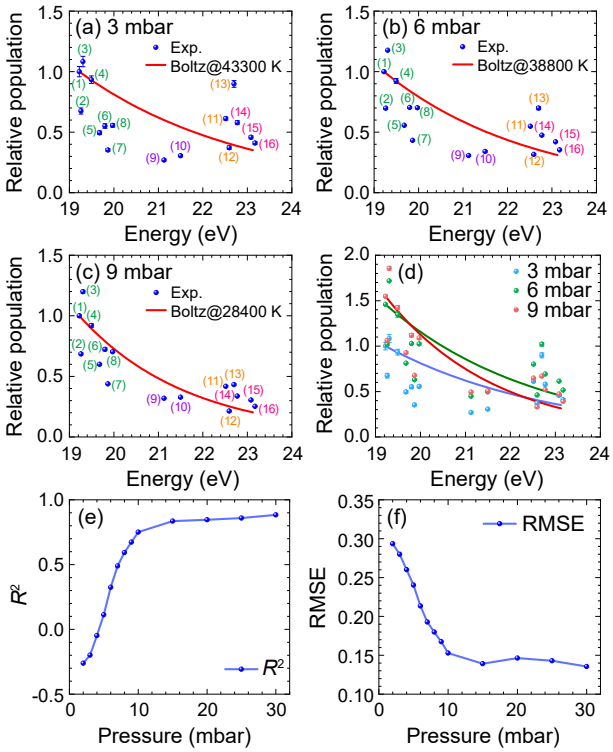

Fig. 5. Relative population distribution of 16 Ar II excited states at 2.2 mJ and gas pressures of (a) 3 mbar, (b) 6 mbar, and (c) 9 mbar. For each pressure, the populations are normalized to that of the 480.60 nm line. The symbols and curves are the same as those in Fig. 4. (d) Relative populations at different gas pressures, normalized to the population of the 480.60 nm line at 3 mbar. (e) R^2 at different pressures. (f) RMSE between fitted and experimental values at different pressures.

trend. This progressive improvement in fitting quality reflects the increasing role of collisional redistribution in driving the population toward Boltzmann equilibrium at higher pressures. Taken together, these results show that gas pressure both promotes post-pulse population redistribution and, at higher pressure, reduces the observable ionic yield.

In summary, we report state-resolved spontaneous-emission spectroscopy of Ar II produced by femtosecond strong-field excitation of argon. Representative ionic lines exhibit a power-law dependence on pulse energy and a non-monotonic dependence on gas pressure. Population analysis based on the selected lines reveals a clear non-Boltzmann distribution that evolves toward a more Boltzmann-like distribution as the gas pressure increases and the pulse energy decreases over the explored range. At comparatively low pressure (e.g., 5 mbar in our measurement), the mean collision interval exceeds the radiative lifetime, and consequently the measured population distribution is expected to be dominated by strong-field preparation, with only a residual collisional contribution. As the pressure increases, the fluorescence signal increasingly reflects the combined influence of pressure-dependent ionic yield and post-pulse collisional redistribution. More broadly, the present work establishes ionic fluorescence as a state-resolved observable for benchmarking nonequilibrium ionic-population models in strong-field laser-atom interaction. Because these populations reflect both the multi-electron channel-specific ionization dynamics and the subsequent collisional and recombinative kinetics, the state-resolved population data presented here may also serve as a quantitative benchmark for multi-electron strong-field calculations, such as time-dependent multi-configuration methods coupled with collisional-radiative models, enabling a direct theory–experiment comparison of ionic-state distributions. Combined with momentum-resolved and ultrafast optical probes, this approach offers a route toward a more complete experimental picture of strong-field ion dynamics.

Acknowledgements

This work was supported by the National Natural Science Foundation of China (Grant Nos. 12234020, 12474281, 12450403, and 12595341) and the Science and Technology Innovation Program of Hunan Province (Grant No. 2025RC3131).

References

[1] Goulielmakis E, Loh Z H, Wirth A, Santra R, Rohringer N, Yakovlev V S, Zherebtsov S, Pfeifer T, Azzeer A M, Kling M F, Leone S R, and Krausz F 2010 *Nature* **466** 739
[2] Ridente E, Hait D, Haugen E A, Ross A D, Neumark D M, Head-Gordon M, and Leone S R 2023 *Science* **380** 713
[3] Zhang Q, Xie H Q, Li G H, Wang X W, Lei H B, Zhao J, Chen Z M, Yao J P, Cheng Y, and Zhao Z X 2020 *Commun. Phys.* **3** 50
[4] Zinchenko K S, Ardana-Lamas F, Seidu I, Neville S P, Van Der Veen J, Lanfaloni V U, Schuurman M S, and Wörner H J 2021 *Science* **371** 489
[5] Chen Y W, Lei H B, Wang Q J, Xie H Q, Zhang H, Lu X, Zhang N, Huang S L, Wu Y Z, Liu J P, Zhang Q, Liu Y, Zhao Z X, Zhao J, and Yao J P 2024 *Phys. Rev. Lett.* **133** 113201
[6] Zhu Y L, Jiang Z Y, Ren Z X, Bai G R, Wang X W, Zhang D W, Liu J L, Zhao J, and Zhao Z X 2024 *Opt. Express* **32** 37446
[7] Corkum P B 1993 *Phys. Rev. Lett.* **71** 1994
[8] Smirnova O, Mairesse Y, Patchkovskii S, Dudovich N, Villeneuve D M, Corkum P B, and Ivanov M Y 2009 *Nature* **460** 972
[9] Williams I D, McKenna J, Wood J, Suresh M, Bryan W A, Stebbings S L, English E M L, Calvert C R, Srigengan B, Divall E J, Hooker C J, Langley A J, and Newell W R 2007 *Phys. Rev. Lett.* **99** 173002
[10] Yuen C H 2026 *Phys. Rev. A* **113** 013125
[11] Chen Y D, Peng S N, Fu Z Y, Qiu L Y, Fan G Y, Liu Y, Wu S J, Xie X H, and Tao Z S 2024 *Commun. Phys.* **7** 1
[12] Wang L, Bai G R, Wang X W, Zhao J, Gao C, Wang J C, Xiao F, Tao W K, Song P, Qiu Q Y, Liu J L, and Zhao Z X 2024 *Nat. Commun.* **15** 2705
[13] Zhao J, Bai G R, Zhang Q, Zhang B, Tao W K, Qiu Q Y, Lei H B, Lang Y, Liu J L, Wang X W, and Zhao Z X 2025 *Phys. Rev. Res.* **7** L012070
[14] Meckel M, Comtois D, Zeidler D, Staudte A, Pavičić D, Bandulet H C, Pépin H, Kieffer J C, Dörner R, Villeneuve D M, and Corkum P B 2008 *Science* **320** 1478
[15] Huismans Y, Rouzée A, Gijsbertsen A *et al* 2011 *Science* **331** 61
[16] Yang Y Z, Hu X Q, Wu L, Wang Z P, Li X K, Zhou S P, Wang Z Z, Guo F M, He L H, Luo S Z, Zhang D D, Wang J G, Chen X J, Wu Y, Wang C C, and Ding D J 2024 *Phys. Rev. Lett.* **133** 113203
[17] Endo T, Otobe T, and Itakura R 2026 *Phys. Chem. Chem. Phys.* **28** 6018
[18] Zhang B 2019 *Chin. J. Chem. Phys.* **32** 35
[19] Chirvi K and Biegert J 2024 *Struct. Dyn.* **11** 041301
[20] Beaulieu S, Bloch E, Barreau L, Comby A, Descamps D, Géneaux R, Légaré F, Petit S, and Mairesse Y 2017 *Phys. Rev. A* **95** 041401
[21] Xu S P, Liu M Q, Hu S L, Shu Z, Quan W, Xiao Z L, Zhou Y, Wei M Z, Zhao M, Sun R P, Wang Y L, Hua L Q, Gong C, Lai X Y, Chen J, and Liu X J 2020 *Phys. Rev. A* **102** 043104
[22] Krausz F and Ivanov M 2009 *Rev. Mod. Phys.* **81** 163
[23] Xiao F, Wang L, Bai G R, Zheng Z G, Sun X, Ji T F, Sun Y C, Wang J C, Wang X W, and Zhao Z X 2025 *Chin. Phys. Lett.* **42** 043701
[24] Wang L, Xiao F, Song P, Tao W K, Sun X, Wang J C, Zheng Z G, Zhao J, Wang X W, and Zhao Z X 2023 *Chin. Phys. Lett.* **40** 114203
[25] Zhang B, Zhao J, and Zhao Z X 2018 *Chin. Phys. Lett.* **35** 043201
[26] Zhang D W, Lü Z H, Meng C, Du X Y, Zhou Z Y, Zhao Z X, and Yuan J M 2012 *Phys. Rev. Lett.* **109** 243002
[27] Wang T J, Xu H L, Daigle J F, Sridharan A, Yuan S, and Chin S L 2012 *Opt. Lett.* **37** 1706
[28] Xu B P, Feng Z Q, Hou J J, Wang S Y, Zhang D C, and Xu H L 2025 *Ultrafast Sci.* **5** 0114
[29] Xu H F, Johnson P M, and Sears T J 2010 *Chin. Phys. Lett.* **27** 083301
[30] Chen Y W, Zhou C H, Lu X, Xu L, Yuan Q, He S Y, Gong R Y, Zhang N, Wang Q J, Huang S L, Wu Y Z, Liu Y, and Yao J P 2024 *Phys. Rev. A* **109** 053522
[31] Zhang X, Lu Q, Zhu Y L, Zhao J, Danylo R, Xu L, Lei M W, Jiang H

B, Wu C Y, Zhang Z D, Houard A, Tikhonchuk V, Mysyrowicz A, Gong Q H, Zhuang S L, Zhao Z X, and Liu Y 2024 *Ultrafast Sci.* **4** 0051
[32] Li H L, Hou M Y, Zang H W, Fu Y, Lotstedt E, Ando T, Iwasaki A, Yamanouchi K, and Xu H L 2019 *Phys. Rev. Lett.* **122** 013202
[33] Yan J L, Chen J T, Liu D, Lian Y, Yao H Q, Wu Q, Lv H, Yan B, and Xu H F 2024 *Chin. J. Chem. Phys.* **37** 737
[34] Wang P, Wu C Y, Lei M W, Dai B, Yang H, Jiang H B, and Gong Q H 2015 *Phys. Rev. A* **92** 063412
[35] Wu C Y, Zhang H, Yang H, Gong Q H, Song D, and Su H M 2011 *Phys. Rev. A* **83** 033410
[36] Yao J P, Li G H, Jia X Y, Hao X L, Zeng B, Jing C R, Chu W, Ni J L, Zhang H S, Xie H Q, Zhang C J, Zhao Z X, Chen J, Liu X J, Cheng Y, and Xu Z Z 2013 *Phys. Rev. Lett.* **111** 133001
[37] Su Q, Sun L, Chu C Y, Zhang Z, Zhang N, Lin L, Zeng Z N, Kosareva O, Liu W W, and Chin S L 2020 *J. Phys. Chem. Lett.* **11** 730
[38] Dogariu A, Michael J B, Scully M O, and Miles R B 2011 *Science* **331** 442
[39] Yao J P, Zeng B, Xu H L, Li G H, Chu W, Ni J L, Zhang H S, Chin S L, Cheng Y, and Xu Z Z 2011 *Phys. Rev. A* **84** 051802
[40] Liu Y, Ding P J, Ibrakovic N *et al* 2017 *Phys. Rev. Lett.* **119** 203205
[41] Lei H B, Yao J P, Zhao J, Xie H Q, Zhang F B, Zhang H, Zhang N, Li G H, Zhang Q, Wang X W, Yang Y, Yuan L Q, Cheng Y, and Zhao Z X 2022 *Nat. Commun.* **13** 4080
[42] Bennett W R, Kindlmann P J, and Mercer G N 1965 *Appl. Opt.* **4** 34
[43] Rudko R I and Tang C L 1967 *J. Appl. Phys.* **38** 4731
[44] Kramida A, Yu Ralchenko, Reader J, and NIST ASD Team 2024 *NIST Atomic Spectra Database*. Version 5.12
[45] Huang T C and Lim G 1985 *Adv. X-Ray Anal.* **29** 461
[46] Schreier F 2019 *J. Quant. Spectrosc. Radiat. Transfer* **226** 87
[47] Aldén M, Westblom U, and Goldsmith J E M 1989 *Opt. Lett.* **14** 305
[48] Rhodes C K 1985 *Science* **229** 1345